CONTROLLING DYNAMIC BRITTLE FAILURE OF POLYMERIC COMPOSITES BY MULTIAXIAL LOADING

Longhui Zhang[1*], David Townsend[1]

[1] Department of Engineering Science, University of Oxford, Parks Road, Oxford, OX1 3PJ, U.K.
* Corresponding author (lhzhang.mechanics@gmail.com &longhui.zhang@eng.ox.ac.uk)

Keywords: Composites, Multiaxial Loading, Brittle-Ductile Transition

ABSTRACT

The syntactic foam and the fibre reinforced polymeric composite are increasingly being conceived for aero engine applications to enhance overall structural reliability under impact loading. The microballon and the fibre contribute to the higher strength of these composites, however, with the potential drawback of brittleness. Studying the brittle behaviour and the method to control the brittleness of these composites under impact loading is of considerable interest to the designers. Systematic compressive tests without and with lateral confinement are conducted to investigate the deformation and failure of epoxy syntactic foam (ESF) and glass fibre reinforced nylon 66 (PA66-GF30) from quasi-static to high strain rates of about 1000/s. The stress–strain relationships of the ESF show significant strain rate dependence. The ESF shows macro elastic-brittle behaviour at high strain rate, and the fracture surface consists of partially deformed and localized regions. With the introduction of lateral confinement, the ESF presents elastic–plastic characteristics. Consequently, the elastic-brittle behaviour of ESF can be suppressed by the lateral confinement. The stress-strain relations of the PA66-GF30 are strain rate and pressure dependent. Beyond maximum stress, micro crack has already formed in dynamically deformed PA66-GF30, which corresponds to macro strain localization. The PA66-GF30 with confinement shows adiabatic shear failure, with fibres coated by severe shear matrix facets and evenly distributed filaments. This is different from the unconfined PA66-GF30 which shows fibres pull out in the fractured matrix.

1 INTRODUCTION

In the aerospace industry, there is an increasing demand in reducing weight and fuel consumption. This requires novel design solutions to reduce the time and cost at the development stage. The syntactic foam, which consists of randomly distributed microballons in the polymeric matrix and owns high strength to weight ratio, is being increasingly used in jet engine fan casing design in the aerospace industries. Likewise, fibre reinforced polymeric composite (FRPC), as a composite made of polymer matrix reinforced with fibres, has also been widely used in aerospace engineering applications. The structural components in service would be subjected to impact loading. The microballon in syntactic foam, and the fibre in FRPC contribute to the higher strength of the composites, however, they also result in brittleness. Evaluation of their dynamic brittle responses and the controlling of their brittleness are of considerable interest to designers.

2 EXPERIMENTAL APPROACH

Systematic compressive tests without and with lateral confinement are carried out to study the deformation and failure of an epoxy syntactic foam (ESF) and glass fibre reinforced nylon 66 (PA66-GF30). As shown in Fig. 1a, the ESF consists of a thermoset epoxy matrix and amorphous silicate-based glass microballons with an average wall thickness of 1.10 μm and an average diameter of about 42 μm. The ratio of the volume occupied by the microballons and the total bulk volume of the foam is approximately 0.5. For PA66-GF30, Fig. 1b shows that the microstructure consists of glass fibres mainly along the longitudinal direction in PA 66 matrix. A closer view of the fibre is given at the top left corner in Fig. 1b.

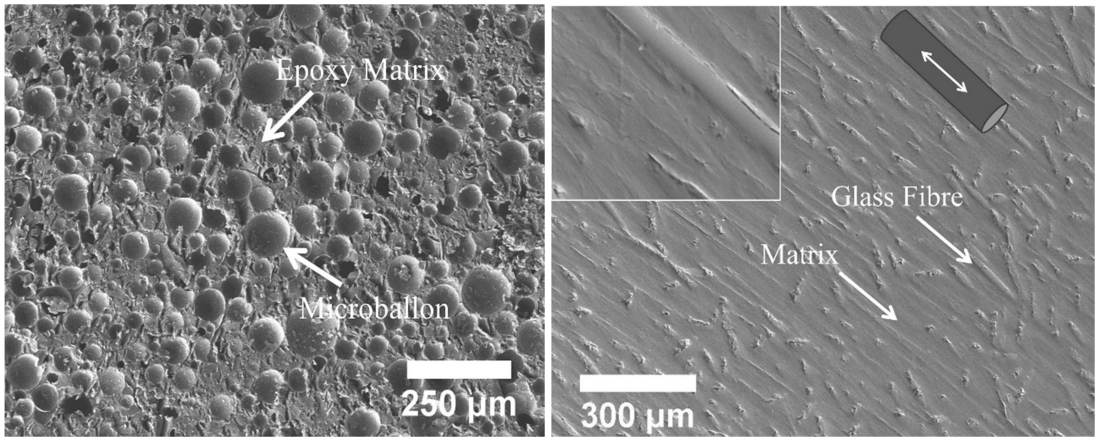

(a) (b)

Figure 1: Initial microstructures of (a) ESF and (b)PA66-GF30. Reprinted from Refs. [1-3].

A thick tube with 3 mm wall thickness and 5 mm internal diameter was manufactured from Ti6Al4V alloy to apply the rigid confinement to the ESF cylinder specimen (5 mm diameter-5mm length). Fig. 2a shows the assembly, with an adapter on top of the confined specimen to apply the compressive loading. Considering the multiaxial loading of PA66-GF30, a thin confining ring made from Al 6061 was used to apply an almost constant confining pressure to the specimen (5 mm diameter-5mm length). The confinement assembly can be seen in Fig. 2b. Different from the foam, the axial loading results in the radial expansion of the PA66-GF30. This causes the plastically yielding Al ring to confined PA66-GF30 specimen. A constant pressure was applied to the specimen from the Al ring designed to be yield at the early stage of the experiment and with a low-strain hardening plastic deformation. The Al rings with different thickness values are designed to obtain low to high confinement conditions.

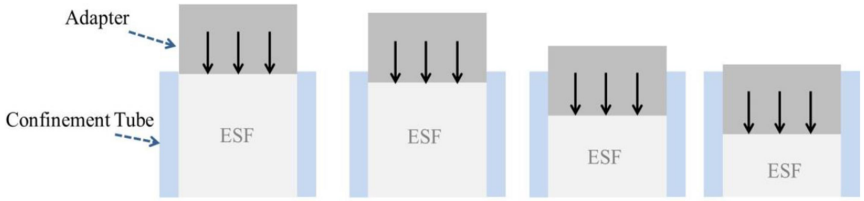

(a)

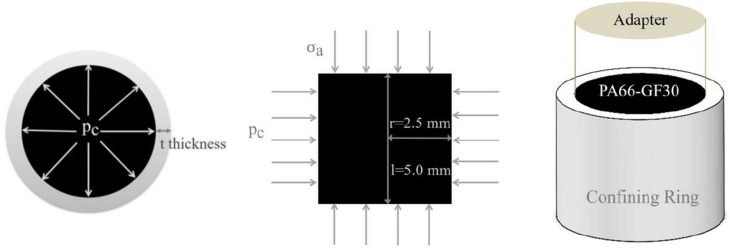

(b)

Figure 2: Schematics of confinement: (a) ESF (b) PA66-GF30. Reprinted from Refs. [1-3].

The compressive tests at quasi-static 0.01 /s and medium strain rate of 10-15 /s were performed using a screw driven Zwick 050 machine and a hydraulic Instron machine 8854, respectively. The relative displacement and the engineering strain of the specimen were measured by two tapes attached on the load platens, with the assistance of commercial DIC software (Lavision Davis). From the camera view, the area of a rectangle in Fig. 3a is the region of interest (ROI) for DIC analysis. The relative displacement is obtained from the strain gauge line function in the software Lavision Davis, in order to measure the engineering strain of the specimen. The true strain can be converted based on the volume constancy. The high strain rate tests (about 1000 /s) were performed using a 16 mm diameter SHPB. Fig. 3b schematically shows the SHPB setup. The incident bar and transmitted bar are made from Ti6Al4V alloy. Both bars are 2.7 m long. The length of the Ti6Al4V strike bar is 2.5 m. The dynamic deformation of the specimen was monitored by using a high speed Kirana camera at a frame rate of 200, 000 fps. The pulse shaper is made from a neoprene rubber sheet with thickness of 0.7 mm-1 mm. The pulse shaper helps to achieve the force equilibrium of the specimen and increases the rise time of the incident wave.

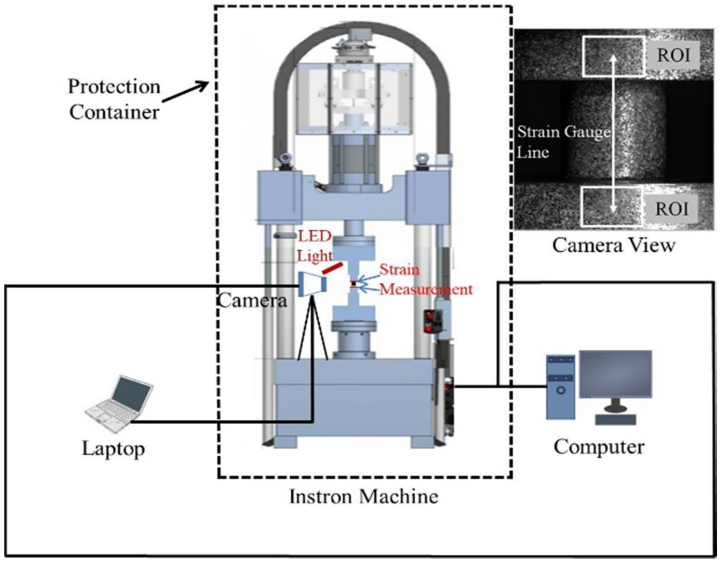

(a)

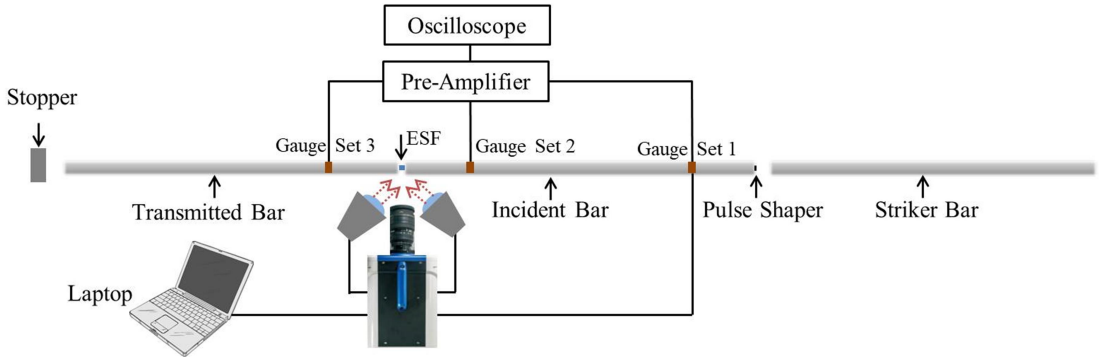

(b)

Figure 3: Test apparatus for (a) medium strain rate and (b) high strain rates. Reprinted from Refs. [1-3].

3 EXPERIMENTAL RESULTS

Fig. 4a shows the engineering stress-strain relationship of the unconfined ESF specimens from quasi-static to high strain rates. The yield stress increases from 52 MPa at 0.01 /s, 58 MPa at 10 /s to 70 MPa at 800 /s. The decrease of stress after the yield stress also shows apparent strain rate dependency. The stress of ESF deforming at high strain rates drops from 70 MPa at the yield stage to 10 MPa at the strain of 0.3, while at medium rates the stress decrease to the value above 30 MPa. The densification stage with increasing stress can still be seen at low strain rates and medium rates, however, the real densification stage of elastic-brittle behavior at high strain rate is absent. Considering the confined engineering stress-strain relationship from low to high rates, Fig. 4b shows that the strain rate effect on the yield stress is apparent, which increases from 52 MPa at 0.01/s, 59 MPa at 10 /s to 74 MPa at 720 /s. All confined stress-strain relationships present elastic-plastic characteristics with significant strain hardening, and the hardening capacity appears not to be apparently strain rate dependent.

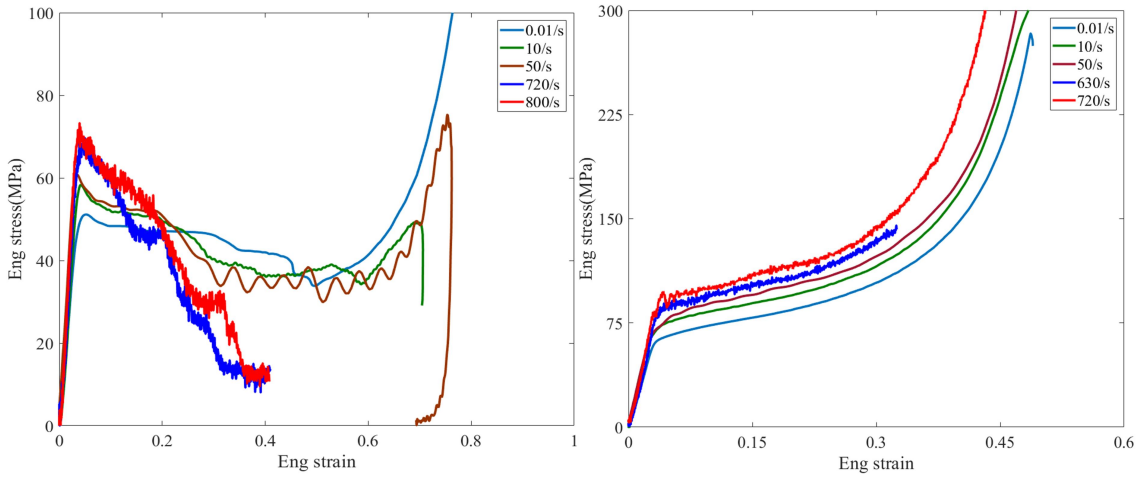

(a) (b)

Figure 4: Engineering stress-strain relationships of (a) unconfined and (b) confined ESF specimens from low to high strain rates. Reprinted from Ref. [2].

Fig. 5a shows the strain rate effect on true stress-strain curves (converted based on the volume constancy) of PA66-GF30 from quasi-static to high strain rates and room temperature. Here, the stress-strain curve at strain rate of 1000 /s was interrupted at a strain level of 0.23 by using a stop ring to control the compressive deformation. The suddenly increasing stress indicates the contact between the Hopkinson bar and the stop ring. Subsequently, the microstructure of recovered specimens was examined to provide further insight into the macro dynamic behaviour with decreasing stress. Beyond maximum stress, micro crack (shown in Ref. [3]) has already formed in dynamically deformed PA66-GF30, which corresponds to macro strain localization. Compared to the responses from quasi-static to high strain rates, it's found that the strain at peak true stress decreases with the increase of strain rate. This indicates that the high strain rate results in a more brittle behaviour of PA66-GF 30. The stress-strain curves at quasi-static and medium strain rates show a longer plateau close to the stress peaks. The stress-strain relationships at high strain rates show higher flow stress but more softening, potentially due to the adiabatic heating effect. Fig. 5b compares the unconfined and confined true stress-strain relationships at high strain rates of 500-700 /s. The low confinement, medium confinement and high confinement corresponding to the confining pressures of 42 MPa, 65 MPa and 86 MPa, which can be achieved using Al rings with various thicknesses at high strain rates. The peak stress increases with the increase of the applied pressure.

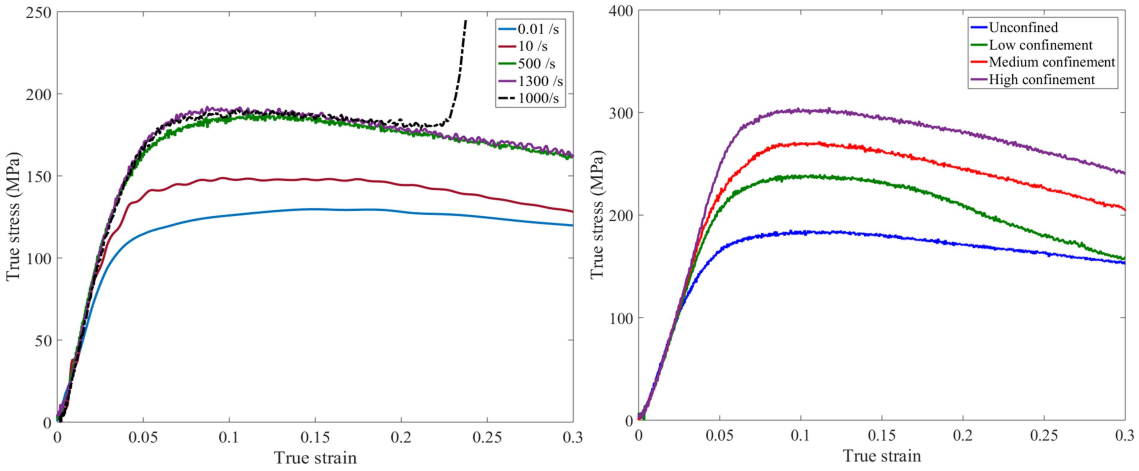

(a) (b)

Figure 5: True stress-strain relationships of (a) unconfined PA66-GF30 from low to high strain rates and (b) confined PA66-GF30 at high strain rates. Reprinted from Ref. [3].

4 MICROSTRUCTURAL CHARACTERIZATION

The fracture morphology of ESF and PA66-GF30 specimens is characterized by using a Carl Zeiss Evo LS 15 VPS canning Electron Microscope. Fig. 6a shows the fracture surface of the unconfined ESF tested at high strain rate, which consists of the partially deformed region and the localized region with collapsed microballons. This corresponds to the strain localization induced brittle failure of the unconfined ESF. Some fractured microballons and the almost intact microballons (white arrow in Fig. 6a) are embedded in the matrix (dashed arrow in Fig. 6a). The confined ESF was constrained inside the rigid tube without failure. Fig. 6b shows the microstructure for the confined ESF under large strain deformation, with the crushed and compacted microballons.

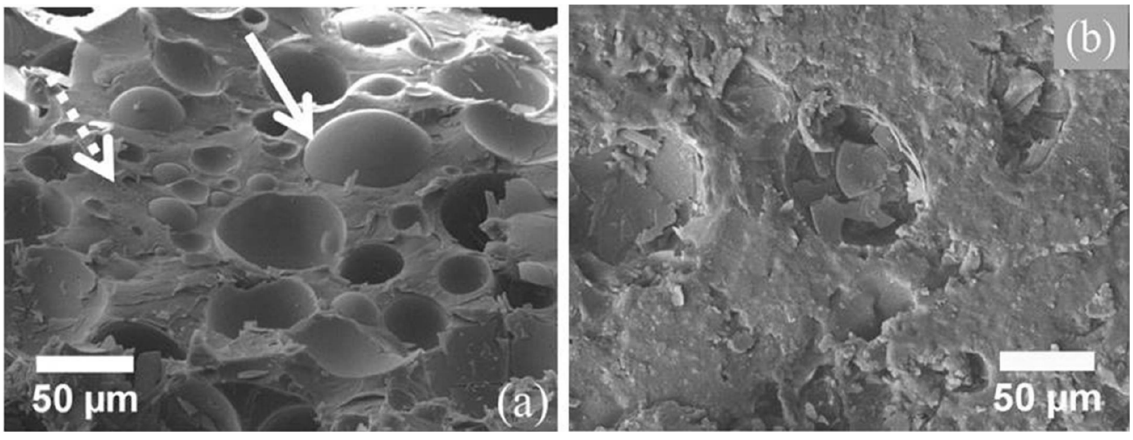

Figure 6: Typical fracture surfaces of unconfined (a) and confined (b) ESF tested at high strain rates and room temperature. Reprinted from Ref. [2].

Fig. 7 compares the dynamic fracture surfaces of PA66-GF30 without and with confinement, with an attempt to illustrate the apparent different fibre-matrix microstructures in unconfined and confined

PA66-GF30. The pulled out fibres (white arrow) in unconfined PA66-GF30 can be seen in Fig. 7a, while they are not apparently visible (white arrow) in Fig. 7b, due to the coating of flow-like behavior of the matrix. The lateral confinement influences the glass fibre-matrix adhesion and interfacial properties. The filaments (white dashed arrows) are distributed on the fracture surface in Fig. 7b. All the above observations point to the significant adiabatic temperature rise during the dynamic deformation with the lateral confinement.

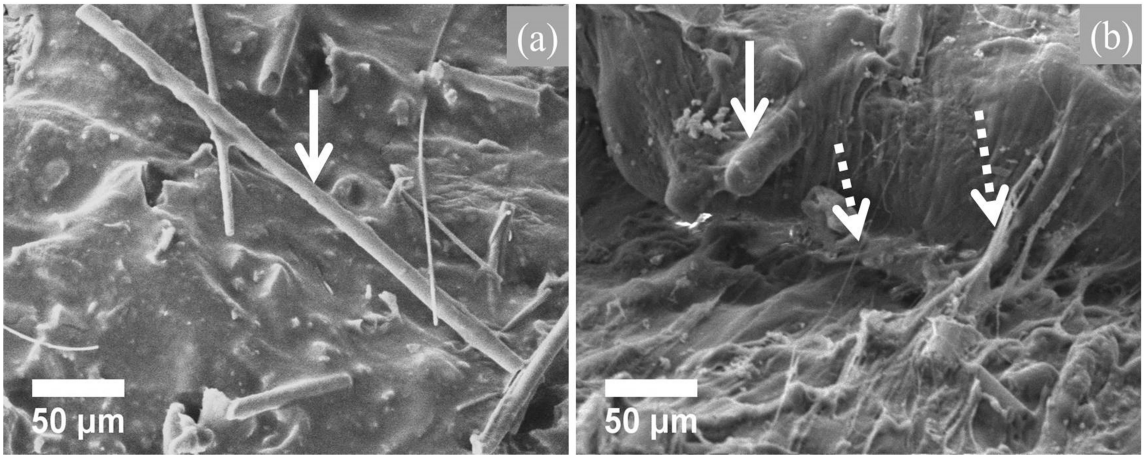

Figure 7: Typical fracture surfaces of (a) unconfined and (b) confined PA66-GF30 tested at high strain rates. Reprinted from Ref. [3].

5 CONCLUSIONS

With the introduction of rigid confinement, the stress-strain relationship of ESF shows elastic-plastic response. The lateral confinement successfully suppresses the elastic-brittle behavior of unconfined ESF at high strain rates. For PA66-GF30, the lateral confinement affects the adhesion between fibre and matrix. Compared to the dynamic failure without confinement, the confined PA66-GF30 presents adiabatic shear failure with the fracture surface consisting of fewer holes from pulled out fibres, which are coated by the flow-like shear matrix due to the adiabatic temperature rise.

ACKNOWLEDGEMENTS

The authors would like to acknowledge Rolls-Royce plc for their continuing support through the University Technology Centre (UTC) at the University of Oxford.

REFERENCES

[1] LH. Zhang, D. Townsend, Strain Rate Dependent Compressive Mechanical Properties and Dynamic Failure of Pre-strained Epoxy Syntactic Foam, Composites Part A, **165**, 2023, 107360.

[2] LH. Zhang, D. Townsend, N. Petrinic, A. Pellegrino, The Dependency of Compressive Response of Epoxy Syntactic Foam on the Strain Rate and Temperature under Rigid Confinement, Composite Structures, **280**, 2022, 114853.

[3] LH. Zhang, D. Townsend, N. Petrinic, A. Pellegrino, Temperature Dependent Dynamic Compressive Response of PA66-GF30 Composite under Constant Strain Rate Multiaxial Loading, Composites Part B, **234**, 2022, 109738.